Applied Numerical Mathematics 59 (2009) 2303–2321

Contents lists available at ScienceDirect

Applied Numerical Mathematics

www.elsevier.com/locate/apnum

Space–time adaptive multiresolution methods for hyperbolic conservation laws: Applications to compressible Euler equations

Margarete O. Domingues [a,c,*], Sônia M. Gomes [b], Olivier Roussel [d], Kai Schneider [c,e]

[a] *Laboratório Associado de Computação e Matemática Aplicada (LAC), Cordenação dos Laboratórios Associados (CTE), Instituto Nacional de Pesquisas Espaciais (INPE), Av. dos Astronautas, 1758, 12227-010 São José dos Campos, Brazil*

[b] *Universidade Estadual de Campinas, IMECC, Caixa Postal 6065, 13083-970 Campinas SP, Brazil*

[c] *Laboratoire de Modélisation en Mécanique Procédés Propres (M2P2), CNRS and Universités d'Aix-Marseille, 38, rue Frédéric Joliot-Curie, 13451 Marseille Cedex 20, France*

[d] *Institut für Technische Chemie und Polymerchemie (TCP), Universität Karlsruhe (TH), Kaiserstr. 12, 76128 Karlsruhe, Germany*

[e] *Centre de Mathématiques et d'Informatique (CMI), Université de Provence, 39, rue Frédéric Joliot-Curie 13453 Marseille Cedex 13, France*

ARTICLE INFO

Article history:
Available online 16 December 2008

Keywords:
Adaptivity
Multiresolution
Finite volume
Runge–Kutta
Partial differential equation
Time step control

ABSTRACT

Adaptive strategies in space and time allow considerable speed-up of finite volume schemes for conservation laws, while controlling the accuracy of the discretization. In this paper, a multiresolution technique for finite volume schemes with explicit time discretization is presented. An adaptive grid is introduced by suitable thresholding of the wavelet coefficients, which maintains the accuracy of the finite volume scheme of the regular grid. Further speed-up is obtained by local scale-dependent time stepping, i.e., on large scales larger time steps can be used without violating the stability condition of the explicit scheme. Furthermore, an estimation of the truncation error in time, using embedded Runge–Kutta type schemes, guarantees a control of the time step for a given precision. The accuracy and efficiency of the fully adaptive method is illustrated with applications for compressible Euler equations in one and two space dimensions.

1. Introduction

Hyperbolic conservation laws, encountered in many applications, such as inviscid compressible flows, exhibit solutions which are typically smooth in large regions of the spatial domain, however they locally present steep gradients or discontinuities. This inhomogeneous spatial behavior motivates the use of adaptive discretizations which allow to resolve the large magnitude of spatial scales without wasting computational resources. Fine grids are hence only used near the steep gradients, while coarser grids are sufficient to represent the solution in smooth regions.

Multiresolution techniques are known to yield an appropriate framework to construct adaptive schemes for hyperbolic conservation laws since the seminal work of Harten [23]. The methods of the present paper fall into this category and aim at combining multiresolution techniques with time adaptivity. In the following we consider three kinds of adaptive strategies to speed up finite volume schemes for time dependent partial differential equations with first order time and space derivatives in one- or two-dimensional Cartesian geometries.

* Corresponding author.
E-mail addresses: margarete@lac.inpe.br (M.O. Domingues), soniag@ime.unicamp.br (S.M. Gomes), roussel@ict.uni-karlsruhe.de (O. Roussel), kschneid@cmi.univ-mrs.fr (K. Schneider).

0168-9274/$30.00 © 2008 IMACS. Published by Elsevier B.V. All rights reserved.
doi:10.1016/j.apnum.2008.12.018

1. **Space adaptivity (MR)**: A second order finite volume scheme (FV) is applied on dynamically adapted grids. We consider space adaptivity in the multiresolution (MR) context of wavelet analysis for cell averages. The main idea of such a MR scheme is to use the decay of the wavelet coefficients to obtain information on local regularity of the solution. Therewith, coarser grids can be used in regions where these coefficients are small **i.e.**, the solution is smooth, while fine grids are used where the coefficients are significant **i.e.**, the solution has strong variations.
2. **Controlled Time Stepping (CTS)**: The time integration is performed with variable time steps, where the time step size selection is based on estimated local truncation errors. The main reason of controlling the error in the solution is to obtain an accurate and safe integration in the whole interval, without the requirement of a fixed time step (or CFL parameter) determined *a priori*. When the estimated local error is smaller than a given tolerance, the code increases the step size to make the integration more efficient.
3. **Local time stepping (LTS)**: The time evolution uses scale-dependent time steps. Instead of evolving the solution with a single time step Δt on all grid cells, computational work is saved by integrating the solution with different time steps, according to each cell scale: if Δt is used for the cells in the finest level, then a double time step $2\Delta t$ is used in the coarser level with double spacing. Required missing values in ghost cells are interpolated in intermediate time levels.

In a recent paper by Ferm and Lötstedt [19], such kinds of adaptive strategies have also being considered for hyperbolic problems in one space dimension. However, instead of MR space adaptivity, there the grid adaptation is based on the control of local discretization errors in space, which are estimated by comparing the space discretization on two different grids. To simplify the data structure, the spatial grids are dynamically refined or coarsened in blocks of grids, in the spirit of the so-called Adaptive Mesh Refinement method [5].

Our purpose in the present paper is to combine the adaptive MR scheme for FV discretization with time step control and local time stepping. Precisely, our goal is to analyze the performance of the following adaptive multiresolution schemes for the simulation of 1D and 2D compressible Euler equations:

- MR: adaptive multiresolution scheme with the same constant time step at each scale;
- MR/CTS: MR scheme with time step control, but the same time step at all scale;
- MR/LTS: MR scheme with scale-dependent local time stepping, but remaining constant in time;
- MR/CTS/LTS: MR scheme with time step control and local time stepping.

The MR scheme belongs to a class of adaptive hybrid methods which are formed by two basic parts: the operational part, and the representation part. The operational part consists of an accurate and stable discretization of the partial differential operators. In the representation part, wavelet tools are employed for the multiresolution organization of the discrete information. A function is discretized at different levels of resolution, which are related by inter-level transformations: projection and prediction operators. The wavelet coefficients are defined as prediction errors, and they retain the detail information when going from a coarse to a finer grid. In particular, these coefficients are small in regions where the solution is smooth and significant close to irregularities. In an adaptive MR method, the goal consists in accelerating a given reference discretization, by taking into account local regularity information indicated by the wavelet coefficients of the numerical solution without deteriorating the quality of the solution.

In the MR context, several methods can be designed, depending on the choices of the representation and operational parts. MR methods were originally introduced for hyperbolic conservations laws by A. Harten [23,24] in the context of finite volume schemes and MR analyses for cell averages. By means of the MR representation of the data, the idea was to reduce the number of costly flux evaluations to speed up the scheme, however without reducing the memory requirements. Harten's approach has been further developed in different directions [1,6,9]. The SPR method, *Sparse Point Representation* was the first fully adaptive MR scheme, introduced by M. Hölmstrom [25,26] in the context of finite differences and interpolating multiresolution analysis, leading to CPU and memory reduction. There the wavelet coefficients are used as regularity indicators to create locally refined grids, on which the numerical solution is represented and the discretization of the operators is performed. Applications of the SPR method have been published in [14,38]. For finite volume discretizations, in combination with cell averaged multiresolution analysis, fully adaptive MR schemes have been developed in [11,21,28,35,39,40]. Discontinuous Galerkin methods have been applied to hyperbolic conservation laws in [8] using Haar wavelet indicators to decide where to refine or coarsen the meshes. These publications reveal that the multiresolution concept has been applied by several groups with success to different stiff problems. For comprehensive literature about the subject, we refer to the books [10,35].

Controlled time stepping is a practice that has been used for a long time in the ODE community [22], with good results. As pointed out by Shampine [41], it is valuable to estimate the error and to monitor the step size in order to get some confidence that the step size is small enough both for resolving the behavior of the solution and for the numerical method to behave as expected. For stiff problems, for which the accuracy requirement can be satisfied with step sizes that are much too large for stability of the numerical method, the control of the local error can be used to stabilize the integration. As described in [42], if the time step is too large for stability, the estimate grows, leading eventually to a step rejection and a reduction of the time step size that will stabilize the method. More recently, CTS schemes have been successfully applied to PDE's [19,27,43]. For hyperbolic flow simulations, the results in [16,19,27] demonstrate the CTS stabilization ability, free of any CFL constraint.

A bottleneck of most of space-adaptive methods, in particular of MR methods, which typically employ explicit or semi–explicit time discretizations, is that the finest spatial grid size imposes a small time step in order to fulfill the stability criterion of the time scheme. Hence, for extensive grid refinement with a huge number of refinement levels, a very small size of the time step is implied. To overcome this difficulty, different strategies have been pursued to introduce adaptive time stepping for adaptive or/and irregular space discretizations of PDEs. For instance, in [13,37,44] local time stepping is analyzed for conservation laws, where the space discretization is non-uniform but fixed. Space–time mesh refinement for the one-dimensional wave equation based on the conservation of a discrete energy is proposed in [12]. In the AMR context, originally proposed by Berger and Oliger [5], local time stepping has been used both for the computation of stationary or non-stationary solutions [4,5,29]. So far, only one-stage time integrations have been used, either explicit or implicit. Recently, multi-stage methods have been considered in the AMR context [19], however, for 1D simulations only. In [18,20,34] local time stepping algorithms for discontinuous Galerkin methods are presented.

In the context of adaptive wavelet methods, Bacry et al. [3] first introduced a scale-dependent time step to 1D test problems. More recently, Müller and Stiriba [36] presented a fully adaptive multiresolution finite volume scheme with a locally varying time stepping. For time discretization, one-stage methods, either explicit or implicit Euler schemes are used. A linear combination, leading to a Crank–Nicholson scheme, yields second order accuracy. Applications for one dimensional conservation laws illustrate the efficiency and accuracy of the scheme. Applications to bidimensional systems are shown in [30,31]. A pure space–time Galerkin approach for viscous Burgers equation where the time axis is treated like a space direction has been introduced by Alam et al. [2]. Results for one space dimension look promising, however the extension of this method to higher dimensions seems questionable as it could be expensive in memory storage.

The methods considered in the present paper are intended to investigate the influence of time adaptive strategies to improve the efficiency of multistage time integration of MR finite volume discretizations applied to compressible Euler equations. For an efficient MR representation, we adopt a data structure which is organized as a dynamic graded tree, as proposed in [40]. In the MR/CTS scheme the time evolution uses a global time stepping, i.e., the same Δt for all cells. However, Δt varies with time, and its size is chosen dynamically. It should be small enough to get a required precision and stability of the computed results, but sufficiently large to avoid unnecessary computational work. In this direction, first results in [16,17] demonstrate the efficiency of the MR/CTS method for typical test problems in 1D and 3D. In the MR/LTS scheme, instead of evolving the solution with a single time step Δt on all grid cells, computational work is saved if the solution is integrated with different time steps, according to each cell scale. In [15], applications of a MR/LTS method, which is validated for 1D test problems to fully adaptive 3D computations for reaction-diffusion equations, illustrate the additional speed-up of such local time-stepping. Compared to previous work, where mostly one stage methods are used, we perform local time-stepping with multistage methods, which becomes technically more difficult as synchronization is required. Finally, the MR/CTS/LTS scheme combines the two time adaptive strategies. In the present paper we apply the different schemes, i.e., MR with fixed time step, MR/CTS and MR/LTS to 2D compressible Euler equations. We also show our first results coupling MR/CTS and MR/LTS.

The paper is organized as follows. In Section 2, we describe the space-adaptive MR finite volume method. The time-adaptive strategies are described in Section 3. In Section 4, the different time-space adaptive MR methods are applied to the compressible Euler equations in one and two space dimensions. The results are compared with the exact solution in 1D and/or with those obtained using the FV, FV/CTS schemes on a regular grid, and the MR scheme with global time stepping. Their accuracy, CPU time and memory compression are discussed. Finally, conclusions of our results and perspectives of this work are drawn in Section 5.

2. Adaptive multiresolution scheme

For the applications of the present paper, we consider a MR method that combines a finite volume discretization for conservation laws with multiresolution analysis for cell averages, in the spirit of the schemes adopted in [11,23,28,35,39].

2.1. Multiresolution representation

The principle in the MR setting is to represent a set of function cell averages as values on a coarser grid plus a series of differences at different levels of nested grids. The differences, i.e., the details, contain the information of the function when going from a coarse to a finer grid level. Adaptive MR representations are obtained by stopping the refinement in a cell at a certain scale level where the wavelet coefficients are insignificant. An efficient way to store the reduced MR data is to use a tree data structure which allows to reduce the memory with respect to a FV scheme on the finest level. Also this kind of representation could increase the speed-up during the time evolution because it reduces the time needed to search for the information of neighbors.

We consider a hierarchy of regular grids in 2D Ω_ℓ, $0 \leqslant \ell \leqslant L$. We denote by $\Omega_{0,(0,0)} = \Omega$ the root cell, which is a rectangle with side lengths h_x and h_y. The different node cells at a level $\ell > 0$ forming Ω_ℓ are given by $\Omega_{\ell,(i,j)}$, where $(i, j) \in \Lambda_\ell$. Here Λ_ℓ denotes the ensemble of indices of the existing node cells on the level ℓ. The $\Omega_{\ell,(i,j)}$ are rectangles with side lengths $h_{x,\ell} = 2^{-\ell} h_x$ and $h_{y,\ell} = 2^{-\ell} h_y$. In the tree terminology, the refinement of a parent node cell $\Omega_{\ell,(i,j)}$ at level ℓ produces four children nodes $\Omega_{\ell+1,(2i,2j)}$, $\Omega_{\ell+1,(2i,2j+1)}$, $\Omega_{\ell+1,(2i+1,2j)}$ and $\Omega_{\ell+1,(2i+1,2j+1)}$ at level $\ell + 1$, as illustrated in Fig. 1.

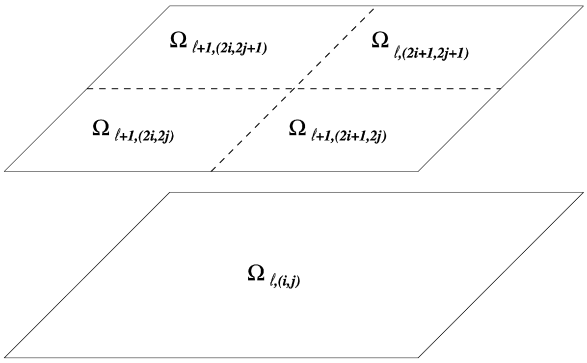

Fig. 1. Dyadic refinement in 2D.

Let $\bar{u}_{\ell,(i,j)} = \frac{1}{|\Omega_{\ell,(i,j)}|}\int_{\Omega_{\ell,(i,j)}} u(x,y)\,dx\,dy$ be the cell-average value of the scalar quantity u on the cell $\Omega_{\ell,(i,j)}$, and $\bar{U}_\ell = (\bar{u}_{\ell,(i,j)})_{(i,j)\in\Lambda_\ell}$ the ensemble of the existing cell-average values at level ℓ. To estimate the cell-averages of a level ℓ from the ones of the level $\ell+1$, we use the projection operator $P_{\ell+1\to l} : \bar{U}_{\ell+1} \mapsto \bar{U}_\ell$. This operator is exact and unique, given that the parent cell-average is nothing but the weighted average of the children cell-averages

$$\bar{u}_{\ell,(i,j)} = \frac{1}{4}\big(\bar{u}_{\ell+1,(2i,2j)} + \bar{u}_{\ell+1,(2i,2j+1)} + \bar{u}_{\ell+1,(2i+1,2j)} + \bar{u}_{\ell+1,(2i+1,2j+1)}\big),$$

To estimate the cell-averages of a level $\ell+1$ from the ones of the level ℓ, we use a prediction operator $P_{\ell\to\ell+1} : \bar{U}_\ell \mapsto \tilde{U}_{\ell+1}$. This operator gives an approximation $\tilde{U}_{\ell+1}$ of $\bar{U}_{\ell+1}$ at the level $\ell+1$. We use the prediction operator of third order given by a tensor product approach [7]. For $n, p \in \{0,1\}$, we define

$$\begin{aligned}\tilde{u}_{\ell+1,(2i+n,2j+p)} = \bar{u}_{\ell,(i,j)} &+ \frac{1}{8}(-1)^n[\bar{u}_{\ell,(i+1,j)} - \bar{u}_{\ell,(i-1,j)}] + \frac{1}{8}(-1)^p[\bar{u}_{\ell,(i,j+1)} - \bar{u}_{\ell,(i,j-1)}]\\ &+ \frac{1}{64}(-1)^{np}\big\{[\bar{u}_{\ell,(i+1,j+1)} - \bar{u}_{\ell,(i+1,j-1)}] - [\bar{u}_{\ell,(i-1,j+1)} - \bar{u}_{\ell,(i-1,j-1)}]\big\}.\end{aligned}$$

Note that this prediction is local, since it is made from the cell average $\bar{u}_{\ell,(i,j)}$ and the eight nearest uncles $\bar{u}_{\ell,(i\pm1,j\pm1)}$. Second, it is consistent with the projection, i.e., $P_{\ell+1\to\ell}\circ P_{\ell\to\ell+1} = \mathrm{Id}$. The details are defined as the difference between the exact and the predicted values at three children cells

$$\begin{aligned}\bar{d}_{\ell+1,(2i,2j+1)} &= \bar{u}_{\ell+1,(2i,2j+1)} - \tilde{u}_{\ell+1,(2i,2j+1)},\\ \bar{d}_{\ell+1,(2i+1,2j)} &= \bar{u}_{\ell+1,(2i+1,2j)} - \tilde{u}_{\ell+1,(2i+1,2j)},\\ \bar{d}_{\ell+1,(2i+1,2j+1)} &= \bar{u}_{\ell+1,(2i+1,2j+1)} - \tilde{u}_{\ell+1,(2i+1,2j+1)}.\end{aligned}$$

Consequently, the knowledge of the cell-average values on the children $\bar{U}_{\ell+1}$ is equivalent to the knowledge of the cell-average values on the parents $\bar{U}_\ell$ and three details

$$\bar{D}_{\ell+1} = \big(\bar{d}_{\ell+1,(2i,2j+1)}, \bar{d}_{\ell+1,(2i+1,2j)}, \bar{d}_{\ell+1,(2i+1,2j+1)}\big)_{(i,j)\in\Lambda_\ell}.$$

Repeating this operation recursively on L levels, one gets the so-called multiresolution transform on the cell-average values [23]

$$\bar{U}_L \longleftrightarrow \big(\bar{D}_L, \bar{D}_{L-1}, \ldots, \bar{D}_1, \bar{U}_0\big).$$

In conclusion, the knowledge of the cell-average values of all the leaves $\bar{U}_L$ is equivalent to the knowledge of the cell-average value of the root $\bar{U}_0$ and the details of all the other nodes of the tree structure.

2.2. Finite volume reference scheme

We consider hyperbolic conservation laws in Cartesian geometry for $(x,y,t) \in \Omega\times[0,+\infty)$, $\Omega\subset\mathbb{R}^2$, of the form

$$\frac{\partial u}{\partial t} = -\nabla\cdot f(u), \tag{1}$$

with initial value $u(x,y,0) = u_0(x,y)$, and appropriate boundary conditions. As reference discretization, we consider numerical solutions represented as vectors $\bar{U} = \bar{U}_L$ containing approximated cell-averages on a uniform grid $\Omega_L = \{\Omega_{L,(i,j)}\}$. For spatial discretization, a finite volume method is adopted which results in an ODE system

$$\frac{d\bar{U}}{dt} = -F(\bar{U}), \tag{2}$$

where $F(\bar{U})$ is the numerical flux function. For accuracy and stability reasons, a TVD second-order accurate scheme, based on an usual upwind scheme is used for space discretization. Here it was decided to choose the AUSM+ scheme [33], together with the Van Albada limiter.

For a sequence of discrete time values $t_n = n\Delta t$, let $\bar{U}^n$ denote an approximation of $\bar{U}$ at t_n. For temporal discretization we use an explicit Runge–Kutta (RK) scheme

$$\bar{U}^* = \bar{U}^n - \Delta t F\big(\bar{U}^n\big), \tag{3a}$$

$$\bar{U}^{n+1} = \frac{1}{2}\big[\bar{U}^n + \bar{U}^* - \Delta t F\big(\bar{U}^*\big)\big]. \tag{3b}$$

The combination of these spatial and temporal discretization may be expressed by a discrete evolution operator $\mathbf{E} = \mathbf{E}(\Delta t)$, such that

$$\bar{U}^{n+1} = \mathbf{E}\bar{U}^n. \tag{4}$$

In the MR scheme, instead of using the representation on the full uniform grid Ω_L, the numerical solution $\bar{U}^n_{MR} = \bar{U}^n_{L,MR}$ is formed by cell averages on an adaptive sparse grid $\Gamma^n = \Gamma^n_L$. Grid adaptivity in the MR scheme is related with an incomplete tree structure, where cell refinement may be interrupted at intermediate scale levels. This means that Γ^n is formed by *leaf cells* $\Omega_{\ell,(i,j)}$, $0 \leqslant \ell \leqslant L$, $i, j \in \mathcal{L}(\Lambda_\ell)$, which are cells without children. Here $\mathcal{L}(\Lambda_\ell)$ denotes the ensemble of indices for the existing leaf cells of the level ℓ.

To evolve the solution from $\bar{U}^n_{MR}$ to $\bar{U}^{n+1}_{MR}$, three basic steps are undertaken:

Refinement: $\bar{U}^{n+}_{MR} \leftarrow \mathbf{R}\bar{U}^n_{MR}$

Evolution: $\check{\bar{U}}^{n+1}_{MR} \leftarrow \mathbf{E}_{MR}\bar{U}^{n+}_{MR}$

Coarsening: $\bar{U}^{n+1}_{MR} \leftarrow \mathbf{T}(\epsilon)\check{\bar{U}}^{n+1}_{MR}$

The refinement operator **R** is a precautionary measure to account for possible translation or creation of finer scales in the solution between two subsequent time steps. Since the regions of smoothness or irregularities of the solution may change with time, the grid Γ^n may not be convenient anymore at the next time step t^{n+1}. Therefore, before doing the time evolution, the representation of the solution should be extended onto a grid Γ^{n+}, which is expected to be a refinement of Γ^n, and to contain Γ^{n+1}. Then, the time evolution operator $\mathbf{E}_{MR} = \mathbf{E}_{MR}(\Delta t)$ is applied. The subscript MR in E_{MR} means that only the cell-averages on the leaves of the computational grid Γ^{n+} are evolved in time, and that an adaptive flux computation $F_{MR}(\bar{U}^{n+}_{MR})$ is adopted at interfaces of cells of different scale levels. Finally, a thresholding operation $\mathbf{T}(\epsilon)$ (coarsening) is applied in order to unrefine those cells in Γ^{n+} that are unnecessary for an accurate representation of $\bar{U}^{n+1}_{MR}$.

If one wants to compress data organized in an adaptive tree structure, while still being able to navigate through it, *graduality* is required. For instance, for a given node in the dynamic tree structure we assume that:

- its parent and the eight nearest uncles are in the tree (if not, create them as nodes);
- for flux computations, if $\Omega_{\ell,(i,j)}$ is a leaf, its eight nearest cousins $\Omega_{\ell,(i\pm p,j)}$ and $\Omega_{\ell,(i,j\pm p)}$, $p \in \{1,2\}$, in each direction are in the tree (if not, create them as virtual leaves);
- if a child node is created, all its brothers are also created.

For more details on these procedures, we refer to [40].

In the tree structure, the thresholding operator $\mathbf{T}(\epsilon)$ is defined by removing leaves where details are smaller than a prescribed tolerance ϵ, while preserving the graduality property, and the refinement operation **R** adds one more level as security zone, in order to forecast the evolution of the solution in the tree representation at the next time step. These two operations are performed by the following procedure.

We denote by Λ the ensemble of indices of the existing tree nodes in Γ^{n+}, by $\mathcal{L}(\Lambda)$ the restriction of Λ onto the leaves, and by Λ_ℓ the restriction of Λ to a level ℓ, $0 \leqslant \ell < L$. For the whole tree, from the leaves to the root:

- Compute the details on the nodes $\bar{d}_{\ell,(i,j)}$, $(i,j) \in \Lambda_{\ell-1}$ by multiresolution transform;
- If the details on a given node and its brothers are smaller than the prescribed tolerance, define this node as deletable.

For the whole tree, from the leaves to the root:

- If a node and its children nodes are deletable, and the children nodes are simple leaves (i.e., without virtual children), then delete their children.
- If the node and its parents are not deletable, and it is not at the maximum level, then create the children for this node.

To illustrate the adaptive flux computation, we consider the leaf $\Omega_{\ell+1,(2i+1,2j)}$, sharing an interface with another leaf $\Omega_{\ell,(i+1,j)}$ at a lower scale level, as illustrated in Fig. 2. For the calculation of the outgoing numerical flux on the right

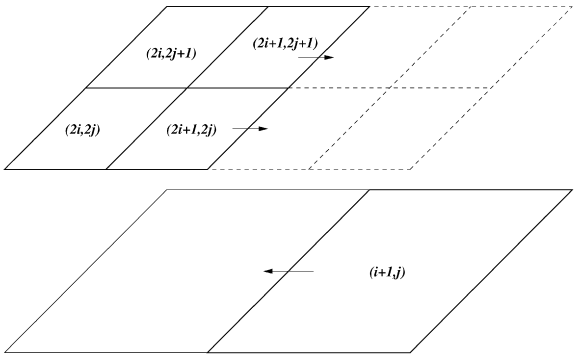

Fig. 2. Adaptive numerical flux computation in 2D.

interface, we use the cell width in the x direction $h_{x,\ell+1}$ as step size. The required right neighboring stencils are obtained from the cousins $\Omega_{\ell+1,(2i+2,2j)}$ and $\Omega_{\ell+1,(2i+3,2j+1)}$, which are virtual cells. For conservation, the ingoing flux on the leaf $\Omega_{\ell,(i+1,j)}$ is set equal to the sum of the outgoing fluxes on the neighbor leaves of level $\ell+1$. For more details on the implementation of this procedure, we refer to [40].

3. Time adaptive strategies for the multiresolution scheme

In the following we consider three time adaptive strategies for the MR scheme.

3.1. MR/CTS scheme

For ODE simulations, instead of using a fixed time step Δt chosen *a priori*, it can be advantageous to have a technique that automatically adjusts its size dynamically. The time step Δt must be chosen sufficiently small to satisfy a required precision of the computed results, denoted by δ_{desired}, but it must be sufficiently large to avoid unnecessary computational work. Typically, if $\bar{U}_{(1)}$ is the approximation of $\bar{U}(t+\Delta t)$, developments of the local truncation errors of the form

$$\bar{U}(t+\Delta t) - \bar{U}_{(1)} = C\Delta t^{p+1} + \mathrm{O}\big(\Delta t^{p+2}\big) \tag{5}$$

could be used to find the step size required to attain a specified accuracy. However, since the leading constant C is not known *a priori*, practical error estimates are necessary. To estimate the local truncation error, one idea is to apply two embedded ODE solvers, one with order p and the other one with order $p+1$ [22,41]. If $\bar{U}_{(2)}$ is the approximation of $\bar{U}(t+\Delta t)$ generated by the method of order $p+1$, then, for sufficiently small Δt we have,

$$\bar{U}_{(1)} - \bar{U}_{(2)} \approx C_1\Delta t^{p+1} - C_2\Delta t^{p+2} \approx C_1\Delta t^{p+1}.$$

This yields the estimate

$$C_1 \approx \frac{\bar{U}_{(1)} - \bar{U}_{(2)}}{\Delta t^{p+1}}.$$

Hence the step size required to maintain the local truncation error of the first scheme below δ_{desired} has the form $\Delta t_{\text{new}} = \xi\Delta t$, where

$$\xi = \left[\frac{\delta_{\text{desired}}}{|\bar{U}_{(1)} - \bar{U}_{(2)}|}\right]^{1/(p+1)}.$$

If we want to prevent the time step of varying too abruptly or to be sure that Δt_{new} in fact will produce an error less than δ_{desired}, some care is needed. In the present implementation, we cannot go back to the previous time step once the solution at the new time step is computed due to the low storage memory model we are using. Hence we decided to limit the variation of the time step by introducing a so–called safety factor ($\mathcal{S}$). The new time step $(\Delta t)_{\text{new}}$ is chosen such that $-\frac{\mathcal{S}}{2} \leqslant \frac{\Delta t_{\text{new}} - \Delta t}{\Delta t} \leqslant \frac{\mathcal{S}}{2}$.

This method is typically used for ordinary differential equations to avoid bad choices of the time step. For memory reasons, we cannot go back in the evolution once we have computed the solution at the new time step, e.g., as proposed by [19]. This means that Δt_{new} is used to evolve the solution to the next step using the higher order scheme. Using a more stringent limiter or a safety factor the choice of non-admissible time steps can be avoided. The drawback of the limiter is that, in case that the initial time step is far from the ideal time step, CPU time could be wasted as the time step cannot be increased sufficiently fast. To overcome this, we heuristically define $\mathcal{S} = \mathcal{S}(t)$ with an exponential decay during the first time steps, i.e.,

$$\mathcal{S}(t) = (\mathcal{S}_0 - \mathcal{S}_{\min}) \exp\left(-\frac{t}{\Delta t}\right) + \mathcal{S}_{\min}.$$

The behavior of the limiter $\mathcal{S}(t)$ for $t = 0$ is the maximal allowed variation $\mathcal{S}_0$ and, for $t \to \infty$, it is $\mathcal{S}_{\min}$, where $\mathcal{S}_{\min} < \mathcal{S}_0$. In the present paper we use $\mathcal{S}_0 = 0.1$ and $\mathcal{S}_{\min} = 0.01$ for all case studies presented. This means that we allow 10% of variation of the time step in the initial time step and after few iterations we allow only 1%.

For the applications of the present paper, we adopt the Runge–Kutta Fehlberg 2(3), where the second order scheme is the one defined in (3). Given $\bar{U}^*$ computed as in (3a), then the third order scheme computes one more stage to obtain

$$\bar{U}^{**} = \frac{1}{4}\left[3\bar{U}^n + \bar{U}^* - \Delta t F\left(\bar{U}^*\right)\right],$$

$$\bar{U}^{n+1} = \frac{1}{3}\left[\bar{U}^n + 2\bar{U}^{**} - 2\Delta t F\left(\bar{U}^{**}\right)\right].$$

In the MR/CTS setting, $\bar{U}$ is replaced by $\bar{U}_{MR}$, and $F(\bar{U})$ should be taken as $F_{MR}(\bar{U}_{MR})$.

3.2. MR/LTS scheme

Assume that, at time t^n, the time step Δt is chosen to evolve the cells at the finest scale level L present in the MR grid (e.g., by the CFL condition or by the CTS procedure). The MR/LTS principle is to evolve the cells at lower levels $0 \leqslant \ell < L$ with time step $\Delta t_\ell = 2^{L-\ell}\Delta t$. The main aspects of such scheme are:

1. One complete time cycle ranges from t^n to t^{n+2^L}.
2. For $0 \leqslant p \leqslant L$, there are intermediate sub-cycles (p, s), from t^{n+s2^p} to $t^{n+(s+1)2^p}$, $0 \leqslant s \leqslant 2^{L-p} - 1$. Thus, $(L, 0)$ corresponds to the complete time cycle.
3. During each sub-cycle (p, s), the time integration is only performed for cells at levels $\ell \geqslant L - p$.
4. Before starting a sub-cycle (p, s), required virtual cell averages should be obtained from the information of their parents, by prediction.
5. Sub-cycle (p, s), starts by the first RK stage for cells at level $L - p$.
6. For those cells which are parents of virtual cells at level $L - p + 1$, cell averages are obtained by linear interpolation at time $t^{n+(2s+1)2^{p-1}}$. Eventually, after the completion of the sub-cycle $(p - 1, 2s)$, and before starting the sub-cycle $(p - 1, 2s + 1)$, these parent cell-averages should be updated by a second RK stage.
7. Next, sub-cycles $(p - 1, 2s)$ and $(p - 1, 2s + 1)$ are performed at levels $\ell \geqslant L - p + 1$.
8. Finally, sub-cycle (p, s) is concluded at time $t^{n+(s+1)2^p}$ after the second RK updating stage for cells at level $L - p$.
9. Refinement operations are only allowed on the tree data structure at level $L - p$, at times $t^{n+(s+1)2^p}$, after the completion of sub-cycle (p, s).
10. Coarsening of the mesh is forbidden during the LTS time cycle.

This procedure is illustrated in Fig. 3, where a MR grid at time t^n contains cells up to the level $L = 2$, and thus the time cycle ranges from t^n to t^{n+4}. Eventually, at the intermediate time t^{n+3}, a grid refinement introduces cells at level 3, and the corresponding cell averages are integrated until the synchronization time t^{n+4}. In practice, several scale levels are allowed in MR grids. However, we recall that, since we are working with a spatially graded tree data structure, there is only one level difference between two neighbor cells. For more details of the implementation of the MR/LTS scheme, we refer to [15].

3.3. MR/CTS/LTS scheme

The MR/CTS/LTS scheme combines the two previous time adaptive strategies as follows:

- First, the MR/CTS strategy is applied just to determine a step size Δt required to safely integrate the problem with a global time stepping.
- Then, the MR/LTS cycle is computed using the obtained step size Δt for the evolution of the cell averages in the finest scale level, and successively larger time steps at coarser levels.
- Finally, another MR/CTS time step is done to adjust the time step after one complete MR/LTS cycle.

This technique hence allows to change the time step size during the time evolution to control the truncation error in time and to benefit from the local time stepping to reduce further the computational cost. Nevertheless, we should mention that the local time stepping implies large time cycles for many refinement levels. The size of the time cycle is increasing with the number of refinement levels. Therefore a wide range of adaptive scales in MR/CTS/LTS implies that the time step control becomes less efficient to rapidly adjust Δt.

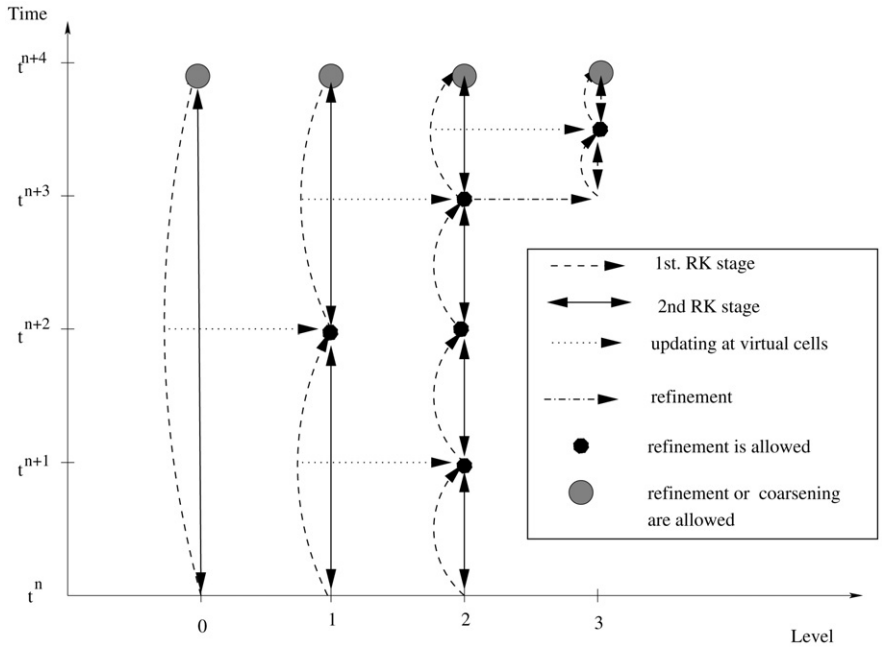

Fig. 3. Illustration of MR/LTS scheme.

4. Applications to Euler equations

To illustrate the accuracy and efficiency of the different MR methods, we consider the compressible Euler equations. In one space dimension, we compute the Lax test-case and in two space dimensions the implosion of an elliptically shaped diaphragm. The results of the adaptive computations are compared with FV computations on the finest grid and for the Lax test-case also with the available exact solution.

4.1. Lax test-case in 1D

We consider the compressible Euler equations

$$\frac{\partial Q}{\partial t} + \frac{\partial F}{\partial x} = 0, \tag{6}$$

with

$$Q = \begin{pmatrix} \rho \\ \rho v \\ \rho e \end{pmatrix} \quad \text{and} \quad F = \begin{pmatrix} \rho v \\ \rho v^2 + p \\ (\rho e + p)v \end{pmatrix}$$

where $\rho = \rho(x,t)$ is the density, $v = v(x,t)$ is the velocity in the x-direction, $e = e(x,t)$ is the energy per unit of mass and $p = p(x,t)$ is the pressure. The system is completed by the equation of state for an ideal gas $p = \rho\mathcal{R}T = (\gamma - 1)\rho(e - v^2/2)$, where $T = T(x,t)$ is the temperature, γ is the specific heat ratio and $\mathcal{R}$ is the specific gas constant. In dimensionless form, we obtain the same system of equations, but the equation of state becomes $p = \rho T/(\gamma Ma^2)$, where Ma denotes the Mach number. For the applications of the present paper, we set $Ma = 1$ and $\gamma = 1.4$.

We consider the Lax test-case corresponding to the initial condition

$$Q(x, t=0) = \begin{pmatrix} 0.445 \\ 0.311 \\ 8.928 \end{pmatrix}, \quad \text{if } x < 0, \quad \text{and} \quad Q(x, t=0) = \begin{pmatrix} 0.5 \\ 0 \\ 1.4275 \end{pmatrix}, \quad \text{otherwise.}$$

Details on this test-case and its exact solution can be found, e.g., in [32,45].

We compute the solution in the domain $\Omega = [-1, 1]$, with Neumann boundary conditions applied on both sides. The simulations are performed until physical time $t = 0.32$, and all errors are taken at this final instant. We take the grid spacing $\Delta x = 2^{L-1}$ at the finest scale level. The results are for $L = 10$ and for the MR schemes the threshold parameter is $\epsilon = 10^{-3}$.

For this problem, the maximal absolute value for the eigenvalues of the Jacobian matrix is constant for $t > 0$, and it is approximately $\lambda_{\max} = 0.47$. Therefore, for all FV, MR and MR/LTS simulations, we assume a constant time step Δt, which is obtained from the input *CFL* parameter by the formula

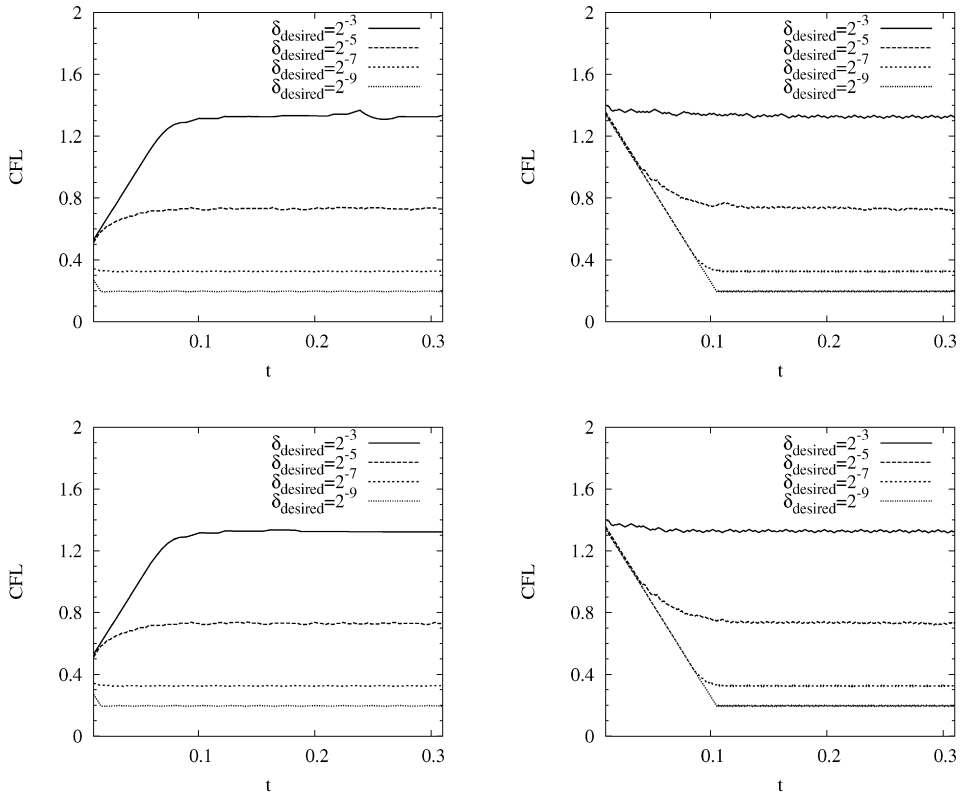

Fig. 4. CFL evolution for FV/CTS (top) and MR/CTS (bottom) schemes, with $CFL(0) = 0.4$ (left) and $CFL(0) = 1.5$ (right).

$$CFL = \lambda_{\max} \frac{\Delta t}{\Delta x}.$$

For FV simulations within $t \leqslant 0.32$ using AUSM + Van Albada limiter and the RK scheme, we found the stability limits $CFL \leqslant 1.0$ for RK2, and $CFL \leqslant 1.33$ for RK3.

For all CTS schemes, an input parameter $CFL(0)$ is provided by the user, and $CFL(t)$ evolves according to the new Δt obtained by time step control. Using the FV/CTS scheme, Fig. 4 (top) shows the CFL evolution for two different values of $CFL(0)$, one below and one above the CFL/RK3 stability limit, namely $CFL(0) = 0.4$, and $CFL(0) = 1.5$. To observe the effect of the δ_{desired} parameter, we consider $\delta_{\text{desired}} = 2^{-M}$, $M = 3, 5, 7,$ and 9. For all cases, initially there is a transient state, and then $CFL(t)$ becomes constant. We find that the steady state value CFL_∞ remains within the stability limit of the scheme. We observe that $CFL_\infty = CFL_\infty(\delta_{\text{desired}})$ decreases when δ_{desired} decreases, but nevertheless it seems to be insensitive to the $CFL(0)$ input. For instance, the plots in Fig. 5 show that, independently of the values $CFL(0) = 0.1, 0.4, 1.0$ and 1.5, the time control strategy forces $CFL(t)$ to stabilize around the constants $CFL_\infty = 0.2, 0.32, 0.72$ and 1.32 for $\delta_{\text{desired}} = 2^{-9}, 2^{-7}, 2^{-5}$ and 2^{-3}, respectively. Similar results hold for the MR/CTS schemes (see Fig. 4, bottom).

To analyze the effect of the CTS strategy on the accuracy of the numerical solution, Table 1 contains L_1 errors for the density at $t = 0.32$ produced by FV/CTS and MR/CTS schemes with different δ_{desired} values. The CPU time of each simulation is also indicated. For comparison, results obtained with the FV-RK3 scheme without time step control are also shown with constant $CFL = CFL_\infty(\delta_{\text{desired}})$. For all cases, the accuracy of the numerical solutions has the same behavior, which is almost insensitive to the CFL history.

Memory and CPU time compression effects of MR, FV/CTS and MR/CTS schemes are given in Table 2. Results are also shown for the L_1 errors on density and kinetic energy, which is defined by

$$E = \frac{1}{2} \int_{-1}^{1} \rho(x) \left| v(x) \right|^2 dx.$$

For the CTS schemes, we choose $\delta_{\text{desired}} = 2^{-3} = 0.125$, which corresponds to $CFL_\infty = 1.32$. We compare three sets of tests: $CFL(0) = 1.5, 0.4$, and 0.1. For the first case, since the initial CFL is above the stability limit, we consider the FV-RK3 scheme with $CFL = 1.32$ as reference scheme. For the second and third cases, the reference scheme is the FV-RK3 scheme with $CFL = CFL(0)$.

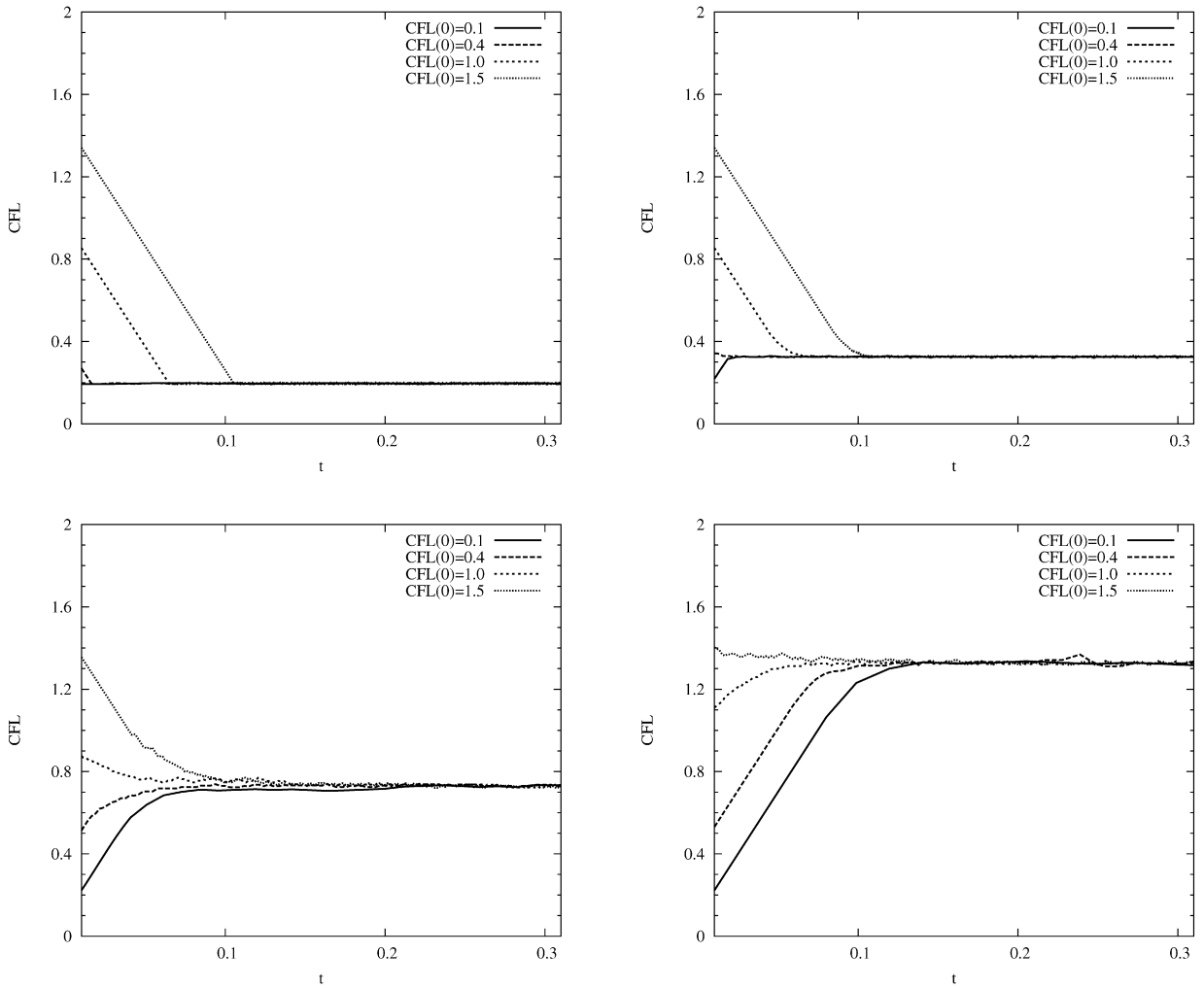

Fig. 5. CFL evolution for the FV/CTS scheme with $\delta_{\text{desired}} = 2^{-9}$ (top, left), 2^{-7} (top, right), 2^{-5} (bottom, left) and 2^{-3} (bottom, right).

Table 1
L_1^{ρ} error ($\times 10^{-3}$) of density ρ and CPU time (sec) for the Lax test-case using FV-RK3, RK2(3) FV/CTS and MR/CTS schemes at time $t = 0.32$ with $L = 10$. For the MR cases $\epsilon = 10^{-3}$ and for the CTS cases $CFL(0) = 0.4$ and 1.5, for different δ_{desired}.

Method, CFL	1.32		0.72		0.32		0.20	
	L_1	CPU	L_1	CPU	L_1	CPU	L_1	CPU
FV-RK3	6.79	28	7.23	51	7.08	115	7.06	183
Method, δ_{desired}	2^{-3}		2^{-5}		2^{-7}		2^{-9}	
for $CFL(0) = 0.4$	L_1	CPU	L_1	CPU	L_1	CPU	L_1	CPU
FV/CTS-RK2(3)	6.75	32	7.08	52	7.09	113	7.09	188
MR/CTS-RK2(3)	7.07	7	7.37	12	7.37	26	7.38	43
for $CFL(0) = 1.5$								
FV/CTS-RK2(3)	6.65	28	7.11	47	7.11	96	7.11	149
MR/CTS-RK2(3)	7.00	5	7.39	9	7.39	19	7.39	30

In all cases, the variation of the L_1 errors is less than 11%, and the errors on the kinetic energy do not exceed 0.18%. All the MR schemes approximately require the same amount of memory, which is less than 40% of the corresponding reference scheme. Concerning CPU time compression with respect to the reference scheme, we observe that the gain is almost the same for the three MR-RK3 computations. However, for the CTS schemes, the gain is more significant, in particular for $CFL(0) = 0.1$ and $CFL(0) = 0.4$. This is an expected behavior, since for these cases $CFL(t)$ increases to $CFL_{\infty} = 1.32$, as shown on the bottom-right side of Fig. 4.

Table 2
Comparison of the speed-up and the errors L_1 on density ρ and energy E for the numerical solution of the 1D Euler equations using the Lax test-case at time $t = 0.32$ with $L = 10$ levels. For every CTS scheme with $\delta_{\text{desired}} = 0.125$. For the MR computations, $\epsilon = 10^{-3}$.

Method	Error		CPU		
	L_1 ($\times 10^{-3}$)	E (%)	Time (sec)	(%)	Memory (%)
FV-RK3, *CFL* = 1.32 (Ref.)	6.79	0.11	28	100	100
FV/CTS-RK2(3), $CFL(0) = 1.5$	6.60	0.16	28	100	100
MR-RK3, $CFL = 1.32$	7.13	0.12	7	25	37
MR/CTS-RK2(3), $CFL(0) = 1.5$	7.00	0.18	5	18	37
FV-RK3, *CFL* = 0.4 (Ref.)	7.05	0.16	91	100	100
FV/CTS-RK2(3), $CFL(0) = 0.4$	6.76	0.17	33	36	100
MR-RK3, $CFL = 0.4$	7.40	0.17	21	23	37
MR/CTS-RK2(3), $CFL(0) = 0.4$	7.07	0.17	7	8	35
FV-RK3, *CFL* = 0.1 (Ref.)	7.05	0.16	368	100	100
FV/CTS-RK2(3), $CFL(0) = 0.1$	6.75	0.17	44	12	100
MR-RK3, $CFL = 0.1$	7.38	0.18	83	22	37
MR/CTS-RK2(3), $CFL(0) = 0.1$	7.04	0.17	9	2	33

Table 3
Comparison of the L_1 error ($\times 10^{-3}$) of density ρ, and CPU time (sec) of the numerical solutions for the Lax test-case using the MR/CTS/LTS-RK2(3) scheme at time $t = 0.32$ with $L = 10$. For the MR cases we use $\epsilon = 10^{-3}$, and for the CTS cases, we use $CFL(0) = 0.4$ and 1.5.

CFL	1.0		0.72		0.32		0.20	
	L_1	CPU	L_1	CPU	L_1	CPU	L_1	CPU
FV-RK2	7.57	25	7.39	35	7.11	78	7.07	126
Method, δ_{desired}	2^{-3}		2^{-5}		2^{-7}		2^{-9}	
for $CFL(0) = 0.4$	L_1	CPU	L_1	CPU	L_1	CPU	L_1	CPU
MR/CTS/LTS-RK2(3)	8.18	5	8.43	9	7.46	19	7.43	32
for $CFL(0) = 1.5$								
MR/CTS/LTS-RK2(3)	8.04	4	8.23	7	7.63	14	7.44	22

The plots for the exact density ρ at $t = 0.32$ and its numerical approximations are shown on the top-left side of Fig. 6 for the third set of schemes presented in Table 2. It is shown that the numerical solutions agree well with the exact one. The three other plots correspond to zoom-ins around the rarefaction zone (Fig. 6, top-right side), the contact discontinuity (Fig. 6, bottom-left side) and the shock (Fig. 6, bottom-right side). In the rarefaction zone and the contact discontinuity, both FV and MR schemes coincide with their CTS version. Due to the thresholding procedure, both MR and MR/CTS computations loose accuracy in these regions, especially in the rarefaction zone, where both FV and FV/CTS schemes almost superimpose with the exact solution. On the other hand, close to the shock, some oscillations appear for the CTS schemes, since for $\delta_{\text{desired}} = 0.125$ these simulations control the CFL parameter around the stability limit. For more restrictive δ_{desired} values, allowing lower stationary CFL values, these oscillations disappear, as shown in Fig. 7.

On the left side of Fig. 8, the leaves of the adaptive MR grid are represented in a position $\times$ scale plane. As expected, the grid is refined close to discontinuities or steep gradients and the highest level is reached in the vicinity of the shock, at the contact discontinuities and at the rarefaction boundaries. The percentage of cells for each scale is presented in Fig. 8. It is shown that the distributions are almost the same for MR-RK3 and MR/CTS-RK2(3) methods tested here. The MR/LTS-RK2 and MR/CTS/LTS-RK2(3) cell distributions also have a similar behavior, but they reaches smaller values around scale 7 than the values obtained with the MR-RK3 and MR/CTS-RK2(3) methods.

All previous computations were also performed with the MR/LTS-RK2 and MR/CTS/LTS-RK2(3). It is shown that the parameter δ_{desired} affects the CFL history in the MR/CTS/LTS-RK2(3) scheme in a very similar way. For instance, the CFL_∞ values coincide with the ones obtained using the MR/CTS scheme (Figs. 4, 5). Furthermore, the MR/CTS/LTS-RK2(3) scheme has the same accuracy as the FV-RK2 scheme with constant $CFL = CFL_\infty(\delta_{\text{desired}})$, as indicated in Table 3.

In Table 4, the L_1 error of density and kinematic energy, together with the memory and CPU time compressions, are shown for the MR/LTS-RK2 and MR/CTS/LTS-RK2(3) schemes with $\delta_{\text{desired}} = 0.125$, the latter corresponding to $CFL_\infty = 1.32$. We compare three sets of tests: $CFL(0) = 1.5, 0.4$, and 0.1. In the first case, for stability reasons, we consider the FV-RK2 scheme with $CFL = 1.0$ as reference scheme. In the second and third cases, the reference scheme is the FV-RK2 scheme with $CFL = CFL(0)$. Concerning CPU time and memory compressions with respect to the FV-RK2 reference scheme, the efficiency of the MR/LTS and MR/CTS/LTS-RK2(3) schemes grows with decreasing initial CFL parameters. Furthermore, the speed-up of the MR/CTS/LTS-RK2(3) scheme with respect to the MR/LTS scheme is also increased from 15% to 36% as $CFL(0)$ decreases from 1.5 to 0.1.

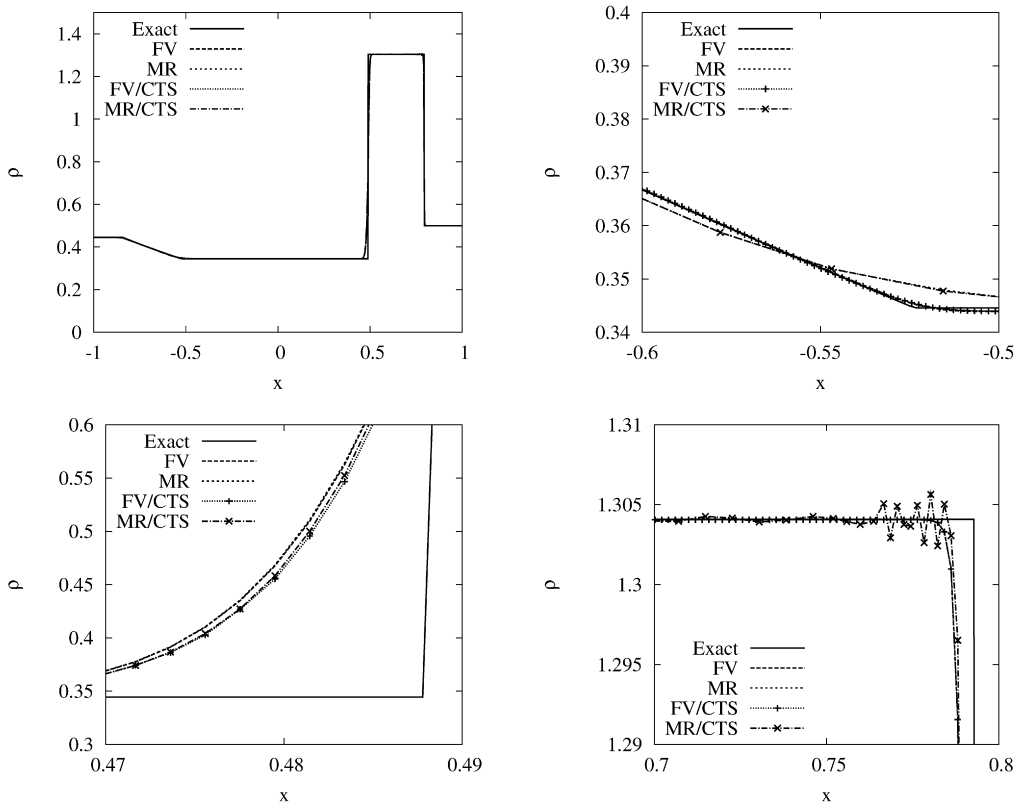

Fig. 6. Exact and computed density for the Lax test-case with the FV-RK3, MR-RK3, FV/CTS-RK2(3), and MR/CTS-RK2(3) schemes, $t = 0.32$ with $L = 10$ (top, left). For all MR cases, $\epsilon = 10^{-3}$, and for all CTS cases, $\delta_{\text{desired}} = 0.125$ and $CFL(0) = 0.1$. Zoom on the rarefaction zone (top, right), the contact discontinuity (bottom, left) and the shock (bottom, right).

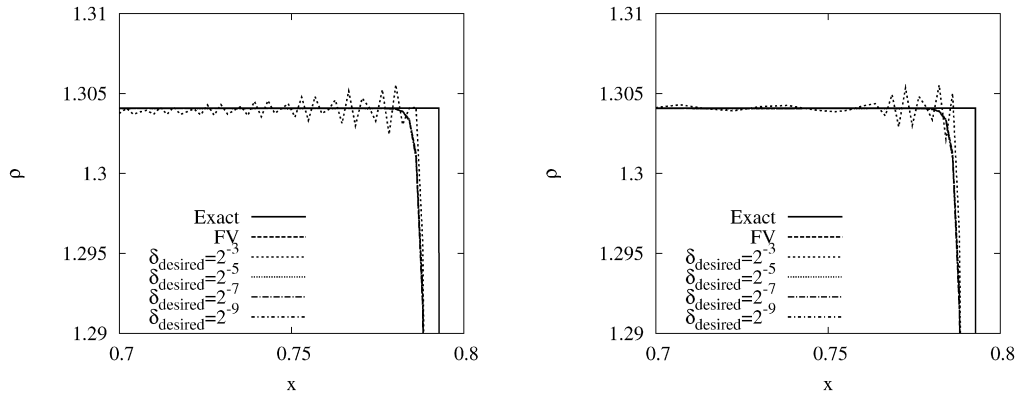

Fig. 7. Zoom on the shock for the FV/CTS-RK2(3) (left) and MR/CTS/LTS-RK2(3) (right) schemes with different δ_{desired}, $CFL(0) = 0.4$. For the MR computations we use $\epsilon = 10^{-3}$.

The plots in Fig. 9 show the exact density profile ρ and its numerical approximations computed with the FV-RK2, MR-RK2, MR/LTS-RK2 and MR/CTS/LTS-RK2(3) schemes close to the contact discontinuity, the shock and the rarefaction wave. In the rarefaction wave region (Fig. 9, top-left side), the best multiresolution approximation is given by the MR-RK2 scheme. On the other hand, the MR/CTS/LTS-RK2(3) solution fits better the lower part of the contact discontinuity (Fig. 9, bottom-right side). Close to the shock, some oscillations also appear for the MR/CTS/LTS-RK2(3) scheme, since for $\delta_{\text{desired}} = 0.125$, this simulation yields a CFL parameter close to the stability limit. These oscillations disappear for more restrictive δ_{desired} values, allowing lower stationary CFL values, as shown in Fig. 10.

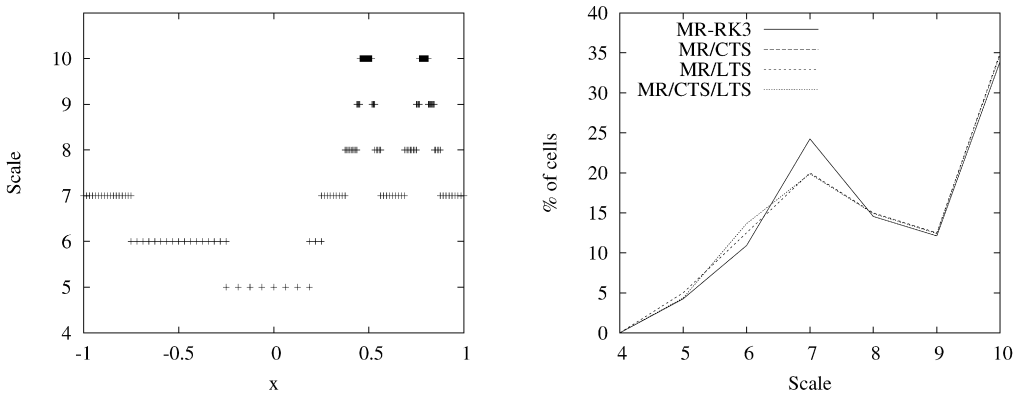

Fig. 8. Adaptive grid (left) and percentage of cells for each scale (right) for the MR method at $t = 0.32$ with $L = 10$, $CFL = 0.1$ and $\epsilon = 10^{-3}$.

Table 4
Comparison of the L_1 error ($\times 10^{-3}$) of density ρ and the energy E, and speed-up of the different numerical schemes applied to the 1D Euler equations at time $t = 0.32$ with $L = 10$ levels. For all CTS schemes computations, $\delta_{\text{desired}} = 0.125$ is used and for the MR computations, we set $\epsilon = 10^{-3}$.

Method	Error		CPU		
	L_1 ($\times 10^{-3}$)	E (%)	Time (sec)	(%)	Memory (%)
FV-RK2, *CFL* = 1.0 (Ref.)	7.57	0.07	25	100	100
MR-RK2, $CFL = 1.0$	7.99	0.08	6	24	37
MR/LTS-RK2, $CFL = 1.0$	7.99	0.08	3	12	37
MR/CTS/LTS-RK2(3), $CFL(0) = 1.5$	8.04	0.10	4	16	35
FV-RK2, *CFL* = 0.4 (Ref.)	7.10	0.15	63	100	100
MR-RK2, $CFL = 0.4$	7.44	0.17	15	24	37
MR/LTS-RK2, $CFL = 0.4$	8.28	0.11	9	14	36
MR/CTS/LTS-RK2(3), $CFL(0) = 0.4$	8.18	0.07	5	8	34
FV-RK2, *CFL* = 0.1 (Ref.)	7.05	0.16	252	100	100
MR-RK2, $CFL = 0.1$	7.44	0.17	58	23	37
MR/LTS-RK2, $CFL = 0.1$	7.43	0.19	44	17	37
MR/CTS/LTS-RK2(3), $CFL(0) = 0.1$	7.94	0.18	13	5	35

4.2. 2D Euler equations: elliptical implosion

As 2D test-case, we study an inviscid implosion phenomenon. In a square box, an elliptic diaphragm separates two regions which contain the same gas, but with different conditions of pressure and temperature. Inside the diaphragm, the pressure and temperature are lower than outside. In both regions, the gas is at rest. On the boundaries, we impose free-slip boundary conditions. The computation is stopped before the shock wave reaches the boundary, so that the influence of the boundaries can be neglected.

At $t = 0$, the diaphragm is broken. A shock wave and a contact discontinuity are moving towards the center, while a rarefaction wave is moving in the opposite direction.

Replacing in (1) the scalar u by the vector of conservative variables $(\rho, \rho v_1, \rho v_2, \rho e)^T$, we obtain the 2D Euler equations in its conservative form. Here ρ is the fluid density, v_1, v_2 are the velocity components in x and y direction, respectively, and e is the energy per unit of mass. The flux function $f = (f_1, f_2)^T$ is given by

$$f_1 = \begin{pmatrix} \rho v_1 \\ \rho v_2^2 + p \\ \rho v_1 v_2 \\ (\rho e + p) v_1 \end{pmatrix}, \qquad f_2 = \begin{pmatrix} \rho v_2 \\ \rho v_1 v_2 \\ \rho v_2^2 + p \\ (\rho e + p) v_2 \end{pmatrix},$$

where the pressure p satisfies $p = (\gamma - 1)\rho(e - \frac{1}{2}(v_1^2 + v_2^2))$, and $\gamma = 1.4$ denotes the specific heat ratio.

The initial condition is defined by $v_1 = v_2 = 0$ and

$$\rho(r, t = 0) = \begin{cases} 1 & \text{if } r \leqslant r_0, \\ 0.125 & \text{if } r > r_0, \end{cases} \qquad \rho e(r, t = 0) = \begin{cases} 2.5 & \text{if } r \leqslant r_0, \\ 0.25 & \text{if } r > r_0, \end{cases}$$

where r_0 denotes the initial radius. The initial condition is stretched in one direction and in addition a rotation is applied. The radius thus becomes $r = \sqrt{X^2/a^2 + Y^2/b^2}$, with the new coordinates $X = x\cos\theta - y\sin\theta$ and $Y = -x\sin\theta + y\cos\theta$.

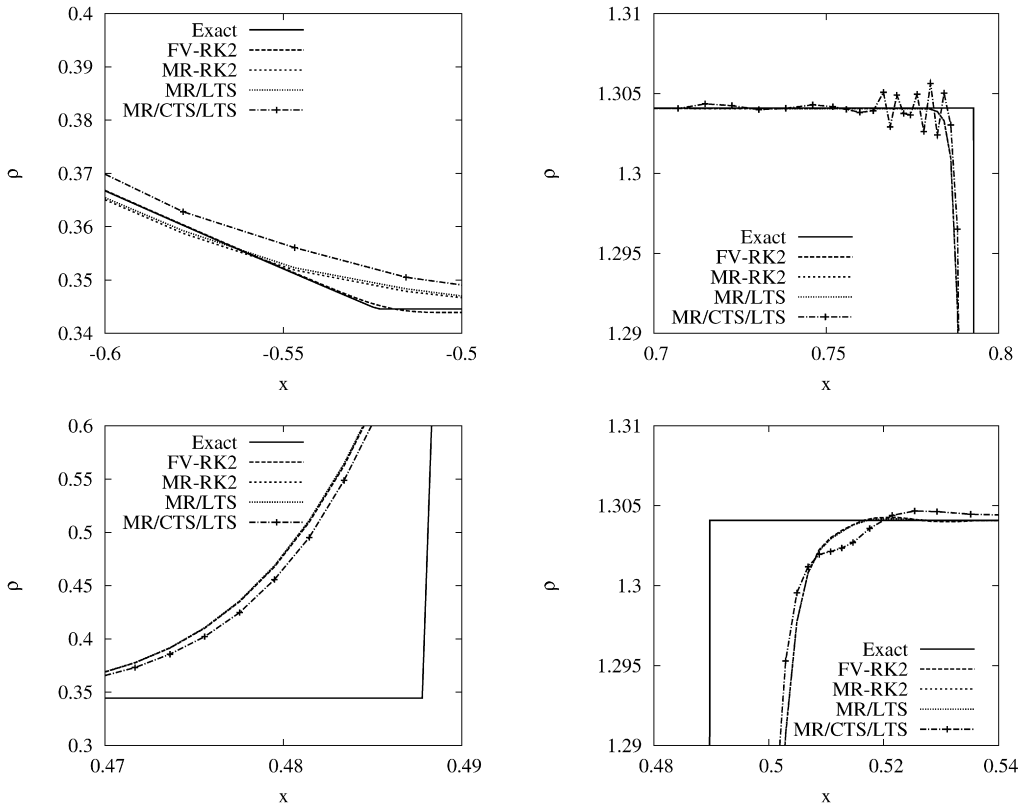

Fig. 9. Exact and computed density for the Lax test-case using the FV-RK2, MR/LTS-RK2, and MR/CTS/LTS-RK2(3) schemes, $t = 0.32$ with $L = 10$. For all MR cases, we use $\epsilon = 10^{-3}$, for all CTS cases, $\delta_{\text{desired}} = 0.125$ and $CFL(0) = 0.1$. Zoom on the rarefaction zone (top, left), the shock region (top, right), and the contact discontinuity region (bottom).

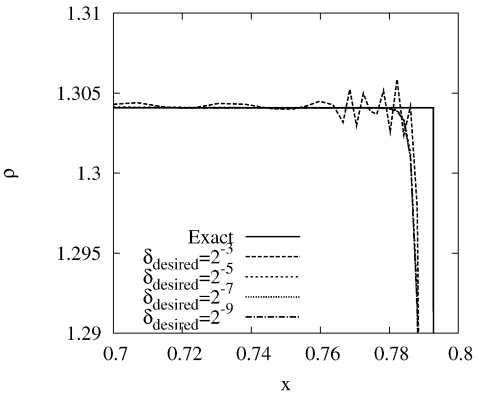

Fig. 10. Zoom on the shock for the MR/CTS/LTS-RK2(3) scheme with $CFL(0) = 0.4$ and different δ_{desired}.

In the following, we choose $a = 1/3$, $b = 1$, $\theta = -\pi/3$, and $r_0 = 1$. The computational domain is $\Omega = [-2, 2]^2$. As before, the numerical flux is computed with the AUSM+ scheme with the van Albada limiter. Either RK2 or RK3 schemes are used for time integration. In all MR computation, the threshold parameter is $\epsilon = 2 \times 10^{-3}$.

To establish the stability limit, the FV scheme is considered with $L = 10$ levels and tested in the time interval $[0, 0.4]$ with a constant time step. The stability limit is given by $CFL(0) \leqslant 0.38$ for the FV-RK2 scheme, and by $CFL(0) \leqslant 0.41$ for the FV-RK3 one. The curves in Fig. 11 represent the time evolution of the CFL for these two limit values, revealing that, during the simulation, $\lambda_{\max}$ reaches a maximum larger than 2.7 times its initial value. Similar behavior is found for the MR computations using both RK2 and RK3 schemes.

Fig. 12 shows the initial isolines of density with the corresponding adaptive grid for $L = 10$. Fig. 13 shows the isolines of density at $t = 0.5$, computed with FV-RK3, MR-RK3, MR/LTS-RK2 and MR/CTS-RK2(3) methods, with $L = 10$ scales. For all tests with a constant time step, we set $\Delta t = 6 \times 10^{-4}$. It corresponds to an initial $CFL(0) = 0.18$. This value has been

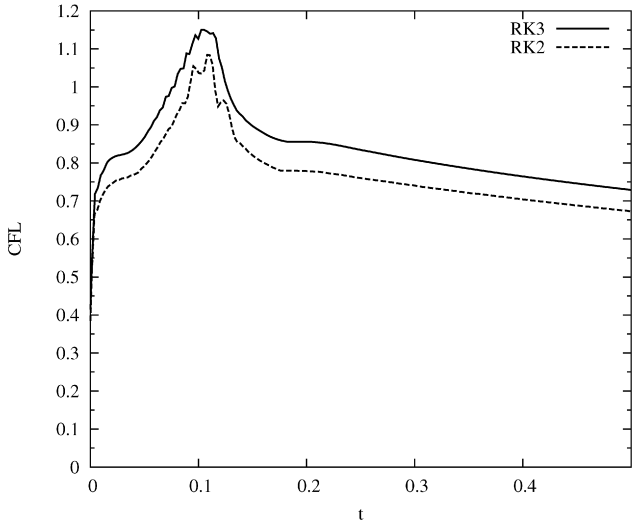

Fig. 11. 2D Euler equations: stability limit for the FV-RK2 and FV-RK3 schemes with constant time step, $L = 10$, $t \leqslant 0.5$.

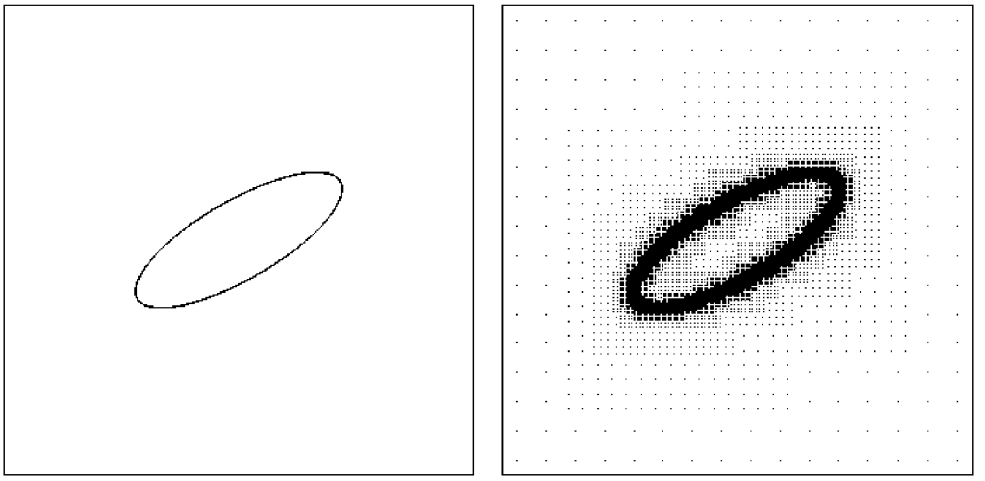

Fig. 12. Initial condition of the 2D Euler equations: density contours (left) and corresponding adaptive grid (right), $L = 10$.

chosen so that $CFL \leqslant 0.5$ during the computation (see Fig. 16). For the CTS schemes, $\delta_{\text{desired}} = 2^{-4}$ and the initial time step is chosen so that $CFL(0) = 0.24$. This value has been chosen so that, for the MR/CTS-RK2(3) scheme, $CFL \leqslant 0.5$ during the computation (see Fig. 16). In Fig. 14, the MR/CTS/LTS-RK2(3) solution is plotted, together with the corresponding adaptive grid. We observe that all the computation fit the FV-RK3 reference solution on the regular finest grid, and that the adaptive grid tracks well the discontinuity and the steep gradients of the solution.

Density cuts are shown in Fig. 15. To check for the grid convergence, we also show the results of a FV computation using one more level ($L = 11$), which corresponds to a resolution of 2048^2. We find a rather good agreement between both FV computations and hence conclude that $L = 10$ levels yield a sufficient resolution for this problem. Concerning the different adaptive MR computations we observe that all computations fit, which is further confirmed by the zooming into the central-right region of the computational domain (Fig. 15, right side).

In Table 5, we compare the computational efficiency and the precision of the different numerical methods using either second or third order time integration schemes. The reference computation is given by the FV scheme on the finest regular grid $L = 11$ with a constant time step corresponding to the initial $CFL(0)$ parameter. For the memory compression, we find for all adaptive schemes approximately the same results, i.e., around 18% of the memory required by the FV computation is used.

To evaluate the accuracy of the computation, we compute the total kinetic energy of the final instant $t = 0.5$ and compare it with the one obtained with the FV-RK3 method computed with one more scale. The best accuracy of the adaptive computation is obtained with the MR/CTS-RK2(3) method, followed by the MR-RK3 and MR/CTS/LTS-RK2(3) methods. However, the difference of accuracy between RK2 and RK3 methods is quite small. The MR/LTS computations show slightly larger errors due to the additional interpolation step. Concerning the speed-up of the adaptive schemes, Table 5 shows

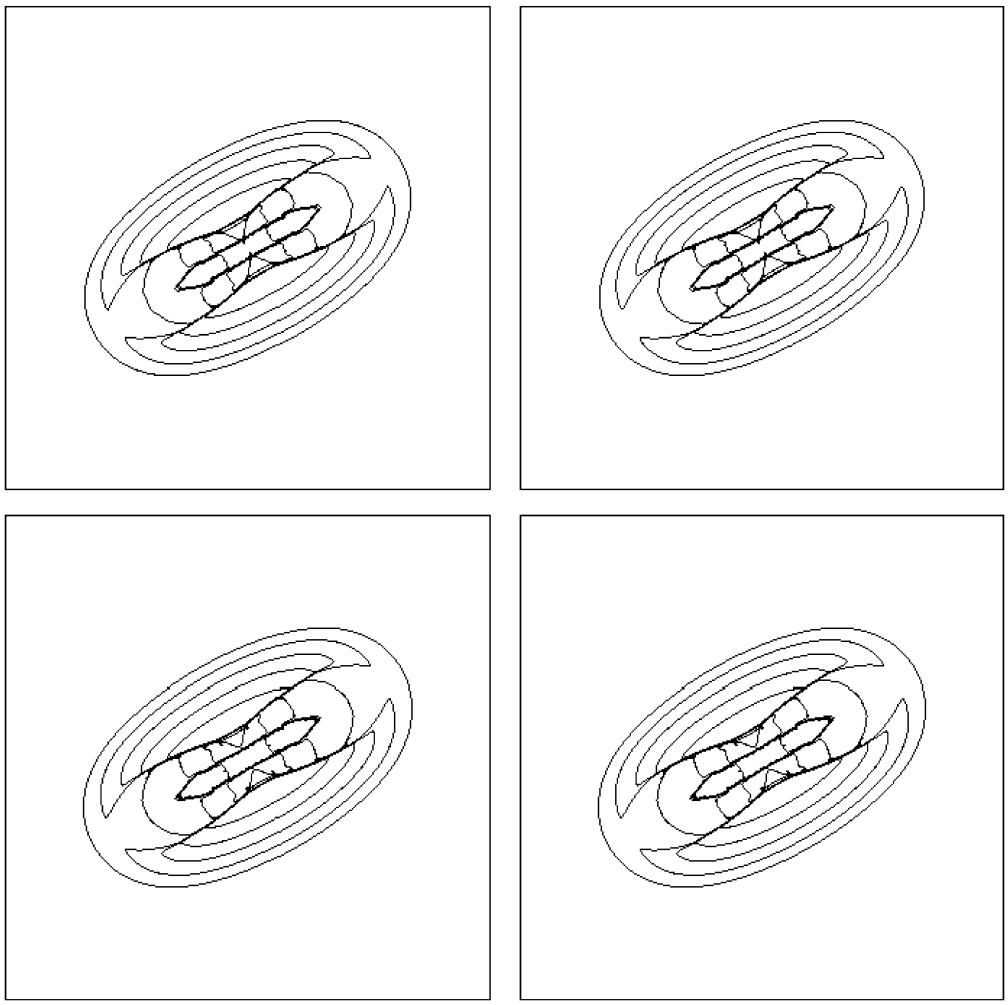

Fig. 13. 2D Euler equations: isolines of density at $t = 0.5$ with $L = 10$, for the FV-RK3 (top, left), MR-RK3 (top, right), MR/CTS-RK2(3) (bottom, left), and MR/LTS-RK2 (bottom, right) methods. We use $\epsilon = 2 \times 10^{-3}$, and we set $\delta_{\text{desired}} = 2^{-4}$.

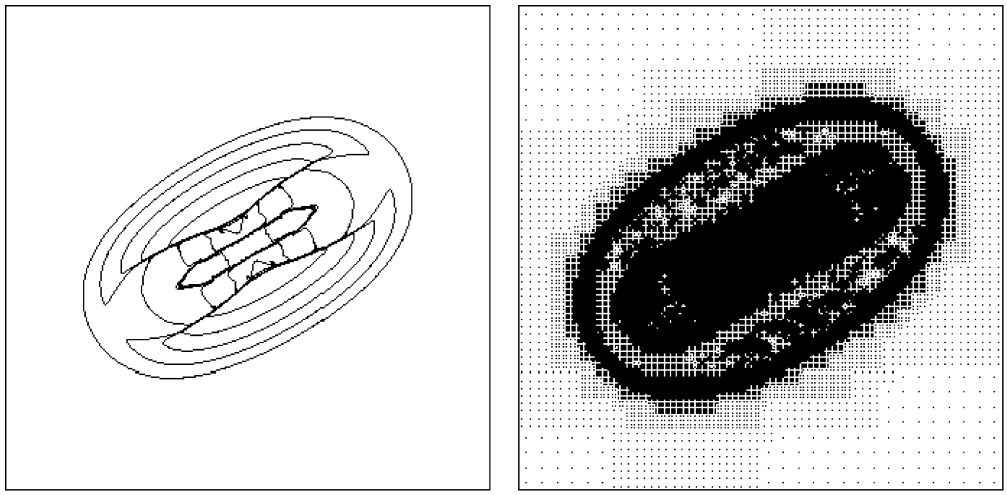

Fig. 14. 2D Euler equations: isolines of density at $t = 0.5$, for the MR/CTS/LTS-RK2(3) method (left), and corresponding adaptive grid (right) with $L = 10$, $\epsilon = 2 \times 10^{-3}$, and $\delta_{\text{desired}} = 2^{-4}$.

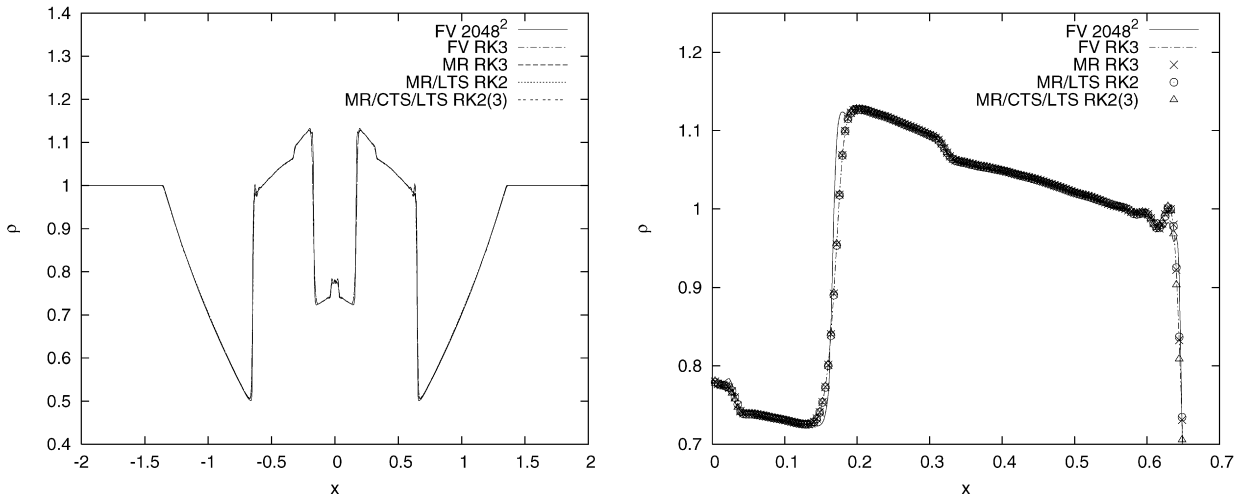

Fig. 15. 2D Euler equations: density profiles for the different methods on the line $y = 0$ at $t = 0.5$ (left), and zoom around the central-right region $[0, 0.7]$ (right) with $L = 10$, $\epsilon = 2 \times 10^{-3}$ and $\delta_{\text{desired}} = 2^{-4}$.

Table 5
Comparison for the numerical solutions of the 2D Euler equations for $t = 0.5$ with $L = 10$ and $\epsilon = 2 \cdot 10^{-3}$.

Method	Error	CPU		
	E (%)	Time	(10^3s ec)	Memory (%)
FV-RK2, ***CFL*(0) = 0.18** (Ref.)	0.60	45	100	100
MR-RK2, $CFL(0) = 0.18$	0.67	10	23	18
MR/LTS-RK2, $CFL(0) = 0.18$	1.09	9	19	16
MR/CTS/LTS-RK2(3), $CFL(0) = 0.24$	0.66	8	18	18
FV-RK3, ***CFL*(0) = 0.18** (Ref.)	0.59	65	100	100
MR-RK3, $CFL(0) = 0.18$	0.66	12	18	18
MR/CTS-RK2(3), $CFL(0) = 0.24$	0.63	9	14	18

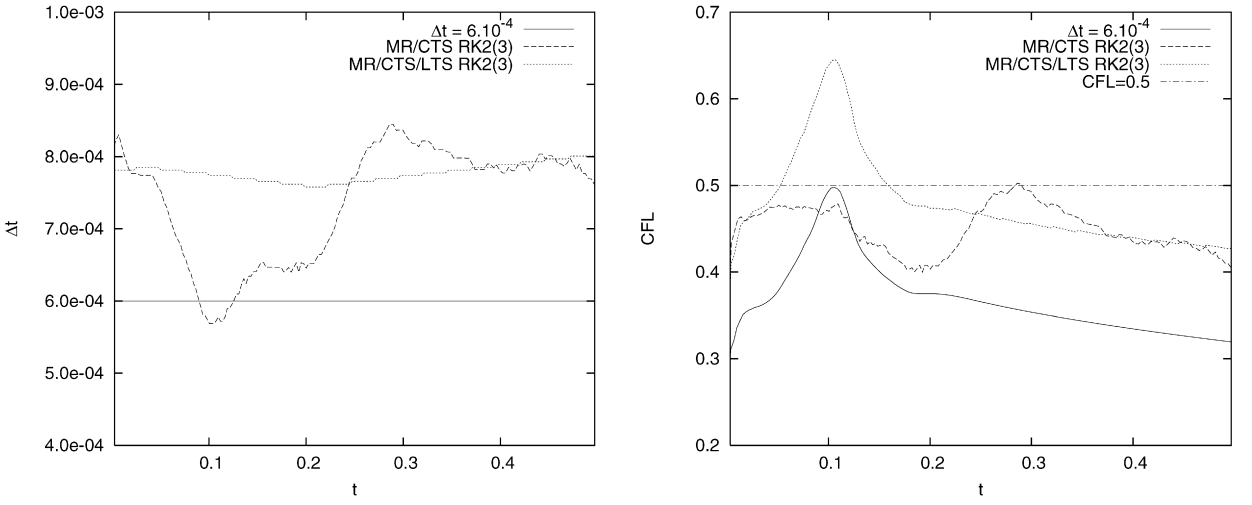

Fig. 16. 2D Euler equations: time evolution of the time step Δt (left) and the CFL number (right) for the different adaptive methods.

that the MR/CTS/LTS-RK2(3) method is 1.5 times faster than the MR-RK3 method, and 8.33 times faster than the FV-RK3 computation, which nicely illustrates the additional speed-up of adaptive and local time stepping.

In Fig. 16, we plot the evolution of the time step, together with the *CFL* number. We observe that all the methods with a fixed time step and the MR/CTS-RK2(3) method guarantee the condition $CFL \leqslant 0.5$. However, the MR/CTS-RK2(3) scheme forces the time step to decrease in the region around $t = 0.1$, where $\lambda_{\max}$ is larger. After $t = 0.2$, for smaller values of $\lambda_{\max}$,

the time step increases again. This behavior illustrates the ability of CTS methods to adapt the step size according to needs of the numerical solution.

For the MR/CTS/LTS-RK2(3) method, the *CFL* locally reaches 0.65, since the time step on the finest grid can only be modified at the end of a time cycle (see Fig. 16, left). Nevertheless, this fact does not affect much the quality of the solution, since the error on the kinetic energy is roughly the same as the one obtained using the MR-RK3 method.

5. Conclusion

In the present paper, different time stepping strategies for space adaptive MR methods for hyperbolic conservation laws were investigated and applied to the compressible Euler equations in one and two space dimensions. We have compared explicit time stepping using a fixed time step with a level-dependent time-stepping MR/LTS method, where the time step can be increased at larger scales without violating the stability criterion, and with a controlled time stepping MR/CTS method, where the time step is automatically adjusted during the time evolution. In addition, we have presented a combination of the two latter methods where, after one complete cycle of the MR/LTS method, a time step control is applied to increase or decrease the current time step.

For both 1D and 2D test-cases, we have found that the MR/CTS/LTS-RK2(3) method represents the best compromise between accuracy and efficiency. Furthermore the MR/CTS/LTS-RK2(3) method is the fastest method for the 2D test-case studied here. This motivates the application of MR/CTS/LTS-RK2(3) to three dimensional problems.

In [15], we applied the MR/LTS scheme to reaction-diffusion equations and found already a good speed-up with respect to the MR scheme. The use of MR/CTS/LTS-RK2(3) will probably allow a larger speed-up and allows in addition an automatic time step control to ensure numerical stability, since the stability limit is generally not known *a priori* for reaction-diffusion problems where the source term is strongly non-linear. In future work, we plan to develop a new level dependent time step control which allows to adapt the time step within a cycle of the level dependent time stepping MR/LTS and hence will permit to control the time step of the MR/LTS scheme instantaneously.

Acknowledgements

M.O. Domingues thankfully acknowledges financial support from the ANR project “M2TFP”.

M.O. Domingues and S. Gomes thankfully acknowledges financial support from Ecole Centrale de Marseille, Fundao de Amparo a Pesquisa do Estado de So Paulo (FAPESP) and The Brazilian Research Council (CNPq). O. Roussel and K. Schneider acknowledge financial support from the FrenchGerman DFGCNRS Research Program “LES and CVS of Complex Flows”. K. Schneider thanks the ANR, project “M2TFP” for financial support.

References

[1] R. Abgrall, Multiresolution analysis on unstructured meshes: applications to CFD, in: B.E.A. Chetverushkin (Ed.), Experimentation, Modelling and Computation in Flow, Turbulence and Combustion, Wiley, 1997.
[2] J. Alam, N.-K.-R. Kevlahan, O. Vasilyev, Simultaneous space–time adaptive wavelet solution of nonlinear partial differential equations, J. Comput. Phys. 214 (2006) 829–857.
[3] E. Bacry, S. Mallat, G. Papanicolaou, A wavelet based space-time adaptive numerical-method for partial-differential equations, RAIRO Math. Modell. Numer. Anal. 26 (1992) 793–834.
[4] M.J. Berger, P. Collela, Local adaptive mesh refinement for shock hydrodynamics, J. Comput. Phys. 82 (1989) 67–84.
[5] M.J. Berger, J. Oliger, Adaptive mesh refinement for hyperbolic partial differential equations, J. Comput. Phys. 53 (1984) 484–512.
[6] B.L. Bihari, Multiresolution schemes for conservation laws with viscosity, J. Comput. Phys. 123 (1996) 207–225.
[7] B.L. Bihari, A. Harten, Multiresolution schemes for the numerical solution of 2-D conservation laws I, SIAM J. Sci. Comput. 18 (2) (1997) 315–354.
[8] J.D. Calle, P.R.B. Devloo, S.M. Gomes, Wavelets and adaptive grids for the discontinuous Galerkin method, Numer. Algorithms 39 (2005) 143–158.
[9] G. Chiavassa, R. Donat, Point value multi-scale algorithms for 2D compressible flow, SIAM J. Sci. Comput. 23 (3) (2001) 805–823.
[10] A. Cohen, Wavelet methods in numerical analysis, in: P.G. Ciarlet, J.L. Lions (Eds.), Handbook of Numerical Analysis, vol. VII, Elsevier, Amsterdam, 2000.
[11] A. Cohen, S.M. Kaber, S. Müller, M. Postel, Fully adaptive multiresolution finite volume schemes for conservation laws, Math. Comp. 72 (2003) 183–225.
[12] F. Collino, T. Fouquet, P. Joly, A conservative space–time mesh refinement method for the 1-D wave equation. I. Construction, Numer. Math. 95 (2) (2003) 197–221.
[13] C. Dawson, R. Kirby, High resolution schemes for conservation laws with locally varying time steps, SIAM J. Sci. Comput. 22 (6) (2001) 2256–2281.
[14] M.O. Domingues, S.M. Gomes, L.M.A. Diaz, Adaptive wavelet representation and differentiation on block-structured grids, Appl. Numer. Math. 47 (2003) 421–437.
[15] M.O. Domingues, S.M. Gomes, O. Roussel, K. Schneider, An adaptive multiresolution scheme with local time-stepping for evolutionary PDEs, J. Comput. Phys. 227 (2008) 3758–3780.
[16] M.O. Domingues, O. Roussel, K. Schneider, On space–time schemes for the numerical solution of PDEs, ESAIM Proc. 16 (2007) 181–194.
[17] M. O. Domingues, O. Roussel, K. Schneider, An adaptive multiresolution method for parabolic PDEs with time control, Int. J. Numer. Meth. Eng., DOI: 10.1002/nme.2501.
[18] M. Dumbser, M. Käser, E. Toro, An arbitrary high order discontinuous Galerkin method for elastic waves on unstructured meshes V: Local time stepping and p-adaptivity, Geophys. J. Int. 171 (2) (2006) 695–717, (23).
[19] L. Ferm, P. Löstedt, Space–time adaptive solutions of first order PDEs, J. Sci. Comput. 26 (1) (2006) 83–110.
[20] J.E. Flaherty, R.M. Loy, M.S. Shephard, B.K. Szymanski, J.D. Teresco, L.H. Ziantz, Adaptive local refinement with octree load balancing for the parallel solution of three-dimensional conservation laws, J. Parall. Dist. Comp. 47 (2) (1997) 139–152.
[21] B. Gottschlich-Müller, S. Müller, Adaptive finite volume schemes for conservation laws based on local multiresolution techniques, in: R. Jeltsch, M. Fey (Eds.), Hyperbolic Problems: Theory, Numerics, Applications, in: Inter. Ser. Numer. Math., ISNM, vol. 129, Birkhäuser Verlag Bassel, Switzerland, Bassel, 1999.

[22] E. Hairer, S.P. Norsett, G. Wanner, Solving Ordinary Differential Equations I. Nonstiff Problems, second ed., Computational Mathematics, vol. 8, Springer, Berlin, 2000.
[23] A. Harten, Multiresolution algorithms for the numerical solution of hyperbolic conservation laws, Comm. Pure Appl. Math. 48 (1995) 1305–1342.
[24] A. Harten, Multiresolution representation of data: a general framework, SIAM, J. Numer. Anal. 33 (3) (1996) 385–394.
[25] M. Holmström, Wavelet based methods for time dependent PDEs, Ph.D. thesis, Uppsala University, 1997.
[26] M. Holmström, Solving hyperbolic PDEs using interpolating wavelets, SIAM J. Sci. Comput. 21 (2) (1999) 405–420.
[27] K. Hörnel, P. Lötstedt, Time step selection for shock problems, Comm. Numer. Meth. Eng. 17 (2001) 477–484.
[28] M. Kaibara, S.M. Gomes, A fully adaptive multiresolution scheme for shock computations, in: E.F. Toro (Ed.), Godunov Methods: Theory and Applications, Kluwer Academic/Plenum Publishers, New York, 2000.
[29] R. Keppens, M. Nool, G. Tóth, T.P. Goedbloed, Adaptive mesh refinement for conservative systems: multi-dimensional efficiency evaluation, Comput. Phys. Comm. 153 (2003) 317–339.
[30] P. Lamby, R. Massjung, S. Müller, Y. Stiriba, Inviscid flow on moving grids with multiscale space and time adaptivity, in: A. Bermudez de Castro, D. Gomez, P. Quintela, P. Salgado (Eds.), Numerical Mathematics and Advanced Applications, Springer, Berlin, Heidelberg, 2006, pp. 831–839.
[31] P. Lamby, S. Müller, Y. Stiriba, Solution of shallow water equations using fully adaptive multiscale schemes, Int. J. Numer. Meth. Fluids 49 (4) (2005) 417–437.
[32] R.J. Leveque, Finite Volume Methods for Hyperbolic Systems, Cambridge University Press, Cambridge, UK, 2002.
[33] M.-S. Liou, A sequel to AUSM: AUSM+, J. Comput. Phys. 129 (1996) 364–382.
[34] F. Lörcher, G. Gassner, C.-D. Munz, A discontinuous Galerkin scheme based on a space–time expansion I. inviscid compressible flow in one space dimension, J. Sci. Comput. 32 (2), 175–199.
[35] S. Müller, Adaptive Multiscale Schemes for Conservation Laws, Lectures Notes in Computational Science and Engineering, vol. 27, Springer, Heidelberg, 2003.
[36] S. Müller, Y. Stiriba, Fully adaptive multiscale schemes for conservation laws employing locally varying time stepping, J. Sci. Comput. 30 (3) (2007) 493–531.
[37] S. Osher, R. Sanders, Numerical approximations to nonlinear conservation laws with locally varying time space grid, Math. Comp. 43 (1983) 321–336.
[38] P. Pinho, M.O. Domingues, P.J. Ferreira, S.M. Gomes, A. Gomide, J.R. Pereira, Interpolating wavelets and adaptive finite difference schemes for solving Maxwell's equations: the effects of gridding, IEEE Trans. Magnetics 43 (2007) 1013–1022.
[39] O. Roussel, K. Schneider, An adaptive multiresolution method for combustion problems: application to flame ball – vortex interaction, Comput. Fluids 34 (7) (2005) 817–831.
[40] O. Roussel, K. Schneider, A. Tsigulin, H. Bockhorn, A conservative fully adaptive multiresolution algorithm for parabolic PDEs, J. Comput. Phys. 188 (2003) 493–523.
[41] L.F. Shampine, Error estimation and control of ODEs, J. Sci. Comput. 25 (112) (2005) 3–15.
[42] L.F. Shampine, A. Witt, Control of local error stabilizes integrations, J. Comput. Appl. Math. 62 (1995) 333–351.
[43] B.P. Sommeijer, L.F. Shampine, G.J. Vewer, An explicit solver for parabolic PDEs, J. Comput. Appl. Math. 88 (3) (1997) 315–326.
[44] H.Z. Tang, G. Warnecke, A class of high resolution schemes for hyperbolic conservation laws and convection–diffusion equations with varying time and space grids, SIAM J. Sci. Comput. 26 (4) (2005) 1415–1431.
[45] P. Wesseling, Principles of Computational Fluid Dynamics, Springer, Berlin, 2001.